# Supplementary Information for
# Chemical environment and occupation sites of hydrogen in Li*M*$O_3$

Thomas Köhler,*[a] Matthias Zschornak,*[ab] Christian Röder,[c] Juliane Hanzig,[a] Günter Gärtner,[a] Tilmann Leisegang,[a] Erik Mehner,[a] Hartmut Stöcker,[a] and Dirk C. Meyer[a]

## S1 *Ab initio* calculations of H defect site in stoichiometric Li*M*$O_3$

Several hydrogen defect sites were calculated by DFT in different cell dimensions to determine the most stable O–H configuration for the stoichiometric Li*M*$O_3$ structures. The postulated positions of HARRINGTON et al.[1] and two additional positions for the occupation of a free octahedral site and the substitutional incorporation on a $V'_{Li}$ site were used as the initial occupation sites for hydrogen. The calculations show that hydrogen occupies a preferred position on an O–O connection line between two oxygen planes, which form a regularly empty octahedron. From the original eight starting positions only four energetically stable models remained within the $1 \times 1 \times 1$ unit cell, however, the defect formation energies for the occupation of an empty octahedral or $V'_{Li}$ site are significantly higher than those of the stable H-1 and H-3 position (see Sec. 3.2). Fig. S1 shows the structural models with higher defect formation energies compared to H-1 and H-3. The H-7 position describes the substitutional occupation of a Li vacancy and H-5 and H-8 represent the occupation of the empty octahedral site. Both models have comparable defect formation energies in $LiNbO_3$ and $LiTaO_3$ (see Tab. 1).

In addition to the initial hydrogen sites within the $1 \times 1 \times 1$ unit cell, combinations of possible coupled defects – based on the stable positions H-1 and H-3 – were calculated (see Fig. S1). These configurations are very similar, but the displacement induced by the first H atom along a connection line between the two O planes modifies the chemical environment of the H defect, which results in corresponding changes in repulsion/attraction for the second hydrogen along with internal stresses induced by the first hydrogen. This favours stability for high H concentrations with a significant effect on the $E_{form}$ value. The combination H-1–H-6 was identified as the most stable configuration of a coupled defect, where the single H-6 position is equivalent to a single H-1 position. It should be noted that for $LiNbO_3$ the scenario with three H defects also shows a higher energy gain than three single hydrogen defects.

Our *ab initio* positions in the stoichiometric lattices are comparable to previous data for $LiNbO_3$[2]. The hydrogen was shown to bond along two O–O planes, with a double well potential on the connection line, which indicates two stable sites. Other positions of the spectroscopic model proposed by HARRINGTON et al.[1] were also calculated, but found to be energetically unfavourable. Furthermore, NAHM et al.[2] have considered the substitutional occupation of $V'_{Li}$ and shown that the trapping energy for the substitutional hydrogen defect at the Li site is very large. They suggest that hydrogen as a substitution is favourably trapped by the Li vacancy. This scenario is discussed in Sec. 4.2.

[a] *Institute of Experimental Physics, TU Bergakademie Freiberg, Leipziger Str. 23, 09599 Freiberg, Germany. E-mail: thomas.koehler@physik.tu-freiberg.de, matthias.zschornak@physik.tu-freiberg.de*
[b] *Institute of Physics, TU Chemnitz, Reichenhainer Str. 70, 09126 Chemnitz, Germany.*
[c] *Institute of Applied Physics, TU Bergakademie Freiberg, Leipziger Str. 23, 09599 Freiberg, Germany.*
* Contributed equally to this work.

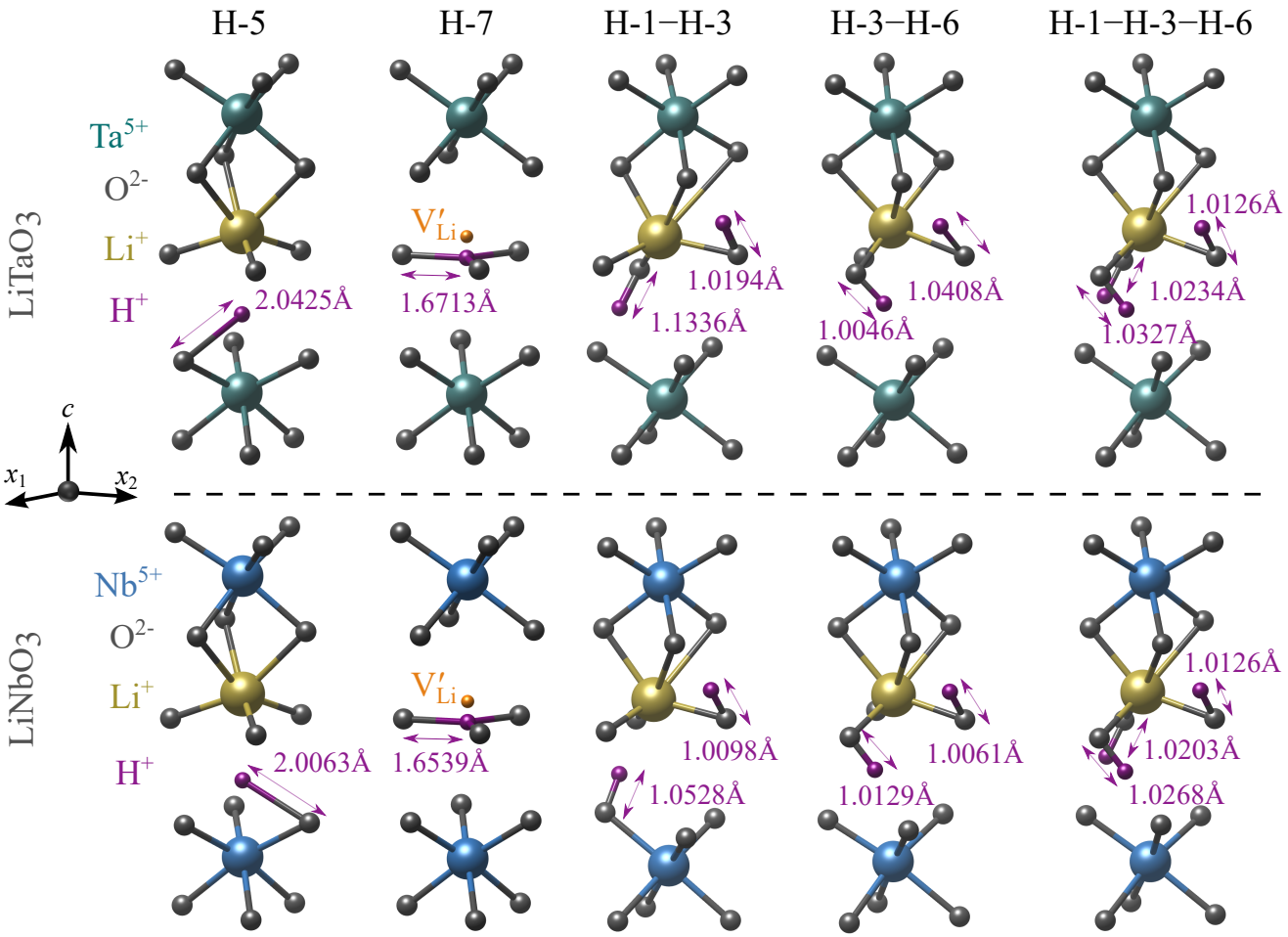


**Fig. S1** Calculated *ab initio* H defect models for $LiTaO_3$ and $LiNbO_3$: comparison of single defect and coupled defect configurations. At high H concentration, the presented coupled models exhibit a lower defect formation energy $E_{form}$ than the calculated H-1 and H-3 models (see Tab. 1 and Fig. 3). The O–H bond lengths to the nearest oxygen neighbour in the relaxed Li*M*$O_3$ structures are indicated.

## S2 Band analysis of NST- and C-Li*M*$O_3$ as-grown crystals

The IR spectra of congruent and near-stoichiometric crystal cubes were analysed using pseudo-VOIGT profiles. The analysis results are summarised in Tab. S1. As already seen from the spectra, the sub-band components of the congruent material are clearly broader and represent a superposition of several components, whereas in the NST material the modes are sharper and separated (see Fig. 4). In agreement with previous data, the $OH^-$ stretching vibration of near-stoichiometric material can be fitted with four sub-bands[3–6]. In contrast, for congruent material a model with two sub-bands is sufficient[1,7–9]. Considering the present results and comparing with near-stoichiometric material, it is assumed that the dominant component $\nu_2$ should consist of at least three components[10]. The overlap of these three contributions depends on the crystal stoichiometry[3,11]. Thus, it is obvious that the components $\nu_{2-4}$ are significantly determined by defects in the material. Crystals with low defect density, such like the investigated as-grown NST-$LiTaO_3$ crystal cubes, exhibit only one sub-band $\nu_1$. The real structure of the congruent crystals changes the chemical environment. This leads to a broadened absorption band. Previous studies reported that component $\nu_2$ cannot be properly fitted by a two-sub-band model, but trying more sub-bands does not provide a clear solution and thus no additional information[10]. The component $\nu_1$ in the congruent material is represented by a small shoulder. Therefore, the standard deviation determined by the band analysis of this component is higher in comparison to the NST material.

The $OH^-$ bands of the congruent material show differences in vibrational contributions of the two components $\nu_1$ and $\nu_2$ and also a difference between the two materials. This difference must be related to a change in the chemical environment, which indicates influences of the real structure. The most significant influence of the real structure is due to the different defect clusters (see Sec. 1). Previous studies determined a $V'_{Li}$ concentration of 5.9 mol% and 2.2 mol% for C-$LiNbO_3$[12] and C-$LiTaO_3$[13], respectively. In addition, previous works[14,15] demonstrated that the defect clusters cause a contraction of the next three oxygen ions as well as a shift of the nearest transition metal ions perpendicular to the *c* axis. Due to this strongly changed chemical environment, there is a strong defect-

related line broadening of the $OH^-$ stretching vibrations[7,16], which is more pronounced in C-$LiTaO_3$ due to the larger interstitial defect cluster (see Tab. S1).

The differences in hydrogen concentration, hydrogen occupation and defect-related line broadening can be assessed from the band analysis. First, a smaller integral band area in as-grown C- and NST-$LiTaO_3$ indicates a lower hydrogen concentration compared to as-grown C- and NST-$LiNbO_3$. The concentration of hydrogen in the structures is obviously coupled to the defect structure. We have calculated lower defect formation energies for $LiNbO_3$ than for $LiTaO_3$, i. e. more hydrogen is found in $LiNbO_3$ (see Sec. 4.2). Second, both material systems show an inhomogeneous occupation of hydrogen bonding sites, as indicated by the $A_{\nu,2}/A_{\nu,1}$ ratio, which is larger for C-$LiTaO_3$. Thus, C-$LiNbO_3$ exhibits a more balanced occupation of the binding sites than C-$LiTaO_3$. It can be assumed for congruent materials that the defect-related component $\nu_2$ is energetically more favourable. Due to the larger Ta interstitial defect cluster in C-$LiTaO_3$, it can be assumed that there is a larger number of chemical environments for a hydrogen decoration than in C-$LiNbO_3$, which contribute to the defect-related inhomogeneous line broadening of the vibrational band[10].

It is generally assumed that the $\nu_1$ component is not coupled to the defect clusters. When the Li content is reduced, this mode decreases and other components appear and dominate the spectrum. Thus, it seems promising that this sub-band can be attributed to an unperturbed occupation site. However, our experimental and theoretical results indicate that this is not the case (see Sec. 3.3.3). In accordance with earlier theoretical calculations[2], the NST material should show a completely different polarisation-dependent behaviour, which is not the case. Therefore, the existing defect model should be extended to include extrinsic defects. According to our model, the growth-induced impurities $Fe^{3+}$ and $Cr^{3+}$ can be regarded as the origin of this vibrational component, since these extrinsic defects cause clustering of the hydrogen near the O–O plane (compare Sec. 4.3 and Fig. 8). The hydrogen clusters preferentially near extrinsic defects on a regular Li site. In agreement with existing literature, the spectroscopic data show that the hydrogen tilts out of the plane by 6° ... 10° for different trivalent dopants[17,18]. In addition to the presented self-compensation of extrinsic defects other charge compensation scenarios are possible and may influence the $OH^-$ tilt and the spectral shape. That the $\nu_1$ mode is weaker for congruent materials can be correlated with the lower concentration of these paramagnetic impurities and the easier compensation of them due to the lithium deficiency (see Sec. S4).

**Table S1** Band analysis of as-grown C- and NST-Li*M*$O_3$ crystal cubes. The IR vibrational bands were fitted with pseudo-VOIGT functions. The analysis yields the peak positions $\nu_i$ ($cm^{-1}$), areas $A_{\nu,i}$ ($cm^{-2}$), FWHMs $\Gamma_{\nu,i}$ ($cm^{-1}$) and shape parameters $\eta_{\nu,i}$. The errors are given in 1$\sigma$ standard deviation.

| Material | $i$ | $\nu_i$ ($cm^{-1}$) | $A_{\nu,i}$ ($cm^{-2}$) | $\Gamma_{\nu,i}$ ($cm^{-1}$) | $\eta_{\nu,i}$ |
|---|---|---|---|---|---|
| C-$LiNbO_3$ | 1 | $3467.05 \pm 0.06$ | $4.79 \pm 0.26$ | $8.46 \pm 0.20$ | $0.61 \pm 0.08$ |
| | 2 | $3484.52 \pm 0.04$ | $70.48 \pm 0.37$ | $25.96 \pm 0.08$ | $0.24 \pm 0.01$ |
| NST-$LiNbO_3$ | 1 | $3465.87 \pm 0.01$ | $15.71 \pm 0.58$ | $4.26 \pm 0.04$ | $0.69 \pm 0.03$ |
| | 2 | $3469.16 \pm 0.29$ | $9.98 \pm 0.48$ | $13.35 \pm 2.44$ | $0.64 \pm 0.04$ |
| | 3 | $3480.07 \pm 0.02$ | $7.68 \pm 0.24$ | $4.65 \pm 0.05$ | $1.00 \pm 0.03$ |
| | 4 | $3489.08 \pm 0.13$ | $1.91 \pm 0.12$ | $7.65 \pm 0.43$ | $0.97 \pm 0.09$ |
| C-$LiTaO_3$ | 1 | $3462.41 \pm 0.08$ | $1.70 \pm 0.31$ | $6.34 \pm 0.23$ | $0.00 \pm 0.42$ |
| | 2 | $3481.15 \pm 0.08$ | $53.44 \pm 0.42$ | $33.04 \pm 0.17$ | $0.06 \pm 0.02$ |
| NST-$LiTaO_3$ | 1 | $3459.71 \pm 0.02$ | $0.52 \pm 0.01$ | $4.01 \pm 0.10$ | $0.89 \pm 0.04$ |

## S3 Hydrogen doping of NST-Li$M$O$_3$

Compared to the congruent crystals, the NST-Li$M$O$_3$ crystals show a significant increase of the $\nu_1$ sub-band after protonation (see Fig. 6). Both crystals display a similar spectral shape of the OH$^-$ vibrational band, which can be fitted with four pseudo-VOIGT profiles. However, the ratios between $\nu_1$ and the other components $\nu_{2-4}$ differ for both NST-Li$M$O$_3$ crystal cubes. Especially the $\nu_1$ component is more pronounced in NST-LiTaO$_3$ than in NST-LiNbO$_3$. This can be attributed to the stoichiometry of the investigated crystals. The NST-LiNbO$_3$ crystals possess a higher Li deficiency with a Li/Nb ratio of 0.988 compared to the NST-LiTaO$_3$ crystals with a Li/Ta ratio of 0.998. Due to the higher intrinsic defect concentration – especially $V'_{Li}$ – these are preferentially decorated and are responsible for the observed $\nu_{2-4}$ vibrational components. This change in the occupation ratios due to the altered chemical environment, can be observed in the $A_{\nu,3}/A_{\nu,1}$ ratio (see Tab. S2), which indicates a preferential occupation of the $\nu_1$ in the NST-LiTaO$_3$. Furthermore, the sub-component $\nu_1$ in NST-LiTaO$_3$ saturates very fast with hydrogen. Thus, after 10 h protonation time, the absorbance of this component is very strong, so that the absorption band is not fully registered and truncated (see. Fig. 6).

To evaluate the $\nu_1$ sub-band with respect to the O–H tilting angles, some crystals were also treated for one hour. The observed vibrational band is now below the upper detection limit and a tilting angle of $\Theta = (6.5 \pm 0.2)^\circ$ can be determined for the investigated NST-LiTaO$_3$, which is comparable to the observed angle for NST-LiNbO$_3$ (see Sec. 3.3.3). For both crystals, this angle is significantly higher than that of the congruent crystals, which proves that the $\nu_1$ sub-band is not connected to the intrinsic defects. Based on our theoretical calculations and the detection of paramagnetic contamination by EPR, we conclude that component $\nu_1$ has its origin in the decoration of extrinsic defects. Thus, the previous description, that $\nu_1$ can be attributed to an undisturbed hydrogen lattice site should be rejected and we propose to correlate $\nu_1$ with the decoration of extrinsic defects. Moreover, the BVEL calculation for the scenario of Cr-doped Li$M$O$_3$ structures has predicted a lower energy barrier for the 3 D hydrogen migration. The spectroscopic data verify that this $\nu_1$ sub-band saturates very quickly, with the highest area increase of all used crystals, when compared to the as-grown materials. Therefore, it can be assumed that the extrinsic defect structure causes a reduction in the diffusion coefficient compared to the intrinsic defect cluster. However, the latter remains to be proven experimentally.

**Table S2** Band analysis of the sub-band components of the OH$^-$ stretching vibrational modes for NST-Li$M$O$_3$ (compare with Fig. 6). The analysis yields the peak positions $\nu_i$ (cm$^{-1}$), areas $A_{\nu,i}$ (cm$^{-2}$), FWHMs $\Gamma_{\nu,i}$ (cm$^{-1}$), shape parameters $\eta_{\nu,i}$ and the area ratio $A_{\nu,3}/A_{\nu,1}$ from fitting two pseudo-VOIGT functions to the entire vibrational bands. The errors are given in 1$\sigma$ standard deviation.

| Material | $i$ | $\nu_i$ (cm$^{-1}$) | $A_{\nu,i}$ (cm$^{-2}$) | $\Gamma_{\nu,i}$ (cm$^{-1}$) | $\eta_{\nu,i}$ | $A_{\nu,3}/A_{\nu,1}$ |
|---|---|---|---|---|---|---|
| NST-LiNbO$_3$ | 1 | 3465.87 ± 0.01 | 15.71 ± 0.58 | 4.26 ± 0.04 | 0.69 ± 0.03 | |
| | 2 | 3469.16 ± 0.29 | 9.98 ± 0.48 | 13.35 ± 0.24 | 0.64 ± 0.04 | |
| | 3 | 3480.07 ± 0.02 | 7.68 ± 0.24 | 4.65 ± 0.05 | 1.00 ± 0.03 | |
| | 4 | 3489.08 ± 0.13 | 1.91 ± 0.12 | 7.65 ± 0.43 | 0.97 ± 0.09 | 0.49 ± 0.03 |
| 1 h prot. NST-LiNbO$_3$ | 1 | 3465.96 ± 0.01 | 66.34 ± 2.55 | 3.02 ± 0.04 | 0.99 ± 0.02 | |
| | 2 | 3468.14 ± 0.33 | 32.09 ± 2.24 | 12.44 ± 0.48 | 0.32 ± 0.06 | |
| | 3 | 3479.78 ± 0.08 | 17.95 ± 2.68 | 6.17 ± 0.33 | 1.00 ± 0.16 | |
| | 4 | 3489.52 ± 0.42 | 3.14 ± 1.18 | 6.36 ± 1.24 | 0.69 ± 0.39 | 0.27 ± 0.05 |
| 10 h prot. NST-LiNbO$_3$ | 1 | 3465.85 ± 0.01 | 80.13 ± 3.07 | 4.17 ± 0.04 | 0.70 ± 0.03 | |
| | 2 | 3468.87 ± 0.26 | 63.16 ± 2.58 | 12.97 ± 0.28 | 0.56 ± 0.02 | |
| | 3 | 3479.87 ± 0.04 | 25.66 ± 2.88 | 5.87 ± 0.22 | 1.00 ± 1.63 | |
| | 4 | 3489.25 ± 0.27 | 5.10 ± 1.06 | 7.24 ± 0.64 | 0.35 ± 0.21 | 0.32 ± 0.05 |
| NST-LiTaO$_3$ | 1 | 3459.71 ± 0.02 | 0.52 ± 0.01 | 4.01 ± 0.10 | 0.89 ± 0.04 | |
| 1 h prot. NST-LiTaO$_3$ | 1 | 3459.50 ± 0.01 | 114.45 ± 2.33 | 3.41 ± 0.02 | 1.00 ± 0.02 | |
| | 2 | 3462.76 ± 0.92 | 23.90 ± 2.30 | 20.00 ± 2.00 | 0.34 ± 0.17 | |
| | 3 | 3474.30 ± 0.16 | 2.01 ± 0.62 | 3.53 ± 0.48 | 0.00 ± 0.37 | |
| | 4 | 3483.00 ± 3.63 | 0.80 ± 1.27 | 11.25 ± 8.00 | 0.00 ± 1.00 | 0.02 ± 0.01 |
| 10 h prot. NST-LiTaO$_3$ | 1 | 3459.82 ± 0.01 | 203.37 ± 7.83 | 4.65 ± 0.05 | 0.78 ± 0.05 | |
| | 2 | 3461.50 ± 0.99 | 35.37 ± 7.26 | 20.26 ± 2.50 | 0.01 ± 0.29 | |
| | 3 | 3474.31 ± 0.12 | 8.87 ± 3.35 | 4.30 ± 0.67 | 0.94 ± 0.33 | |
| | 4 | 3485.36 ± 1.28 | 1.20 ± 1.44 | 7.13 ± 3.39 | 0.13 ± 1.00 | 0.04 ± 0.02 |

## S4 Electron paramagnetic resonance (EPR) spectroscopy

For the EPR measurements, C- and NST-Li$M$O$_3$ single crystal plates were measured with a MS5000 EPR spectrometer (Freiberg Instruments, Freiberg, Germany) at a frequency of 9.46 GHz (X band range), a microwave power of 50 mW and an amplitude modulation of 0.3 mT. All measurements were carried out at room temperature. For data processing, ESRStudio (Bruker BioSpin, Ettlingen, Germany) was used. The presented magnetic field was normalised with respect to the irradiated frequency and the baseline was corrected.

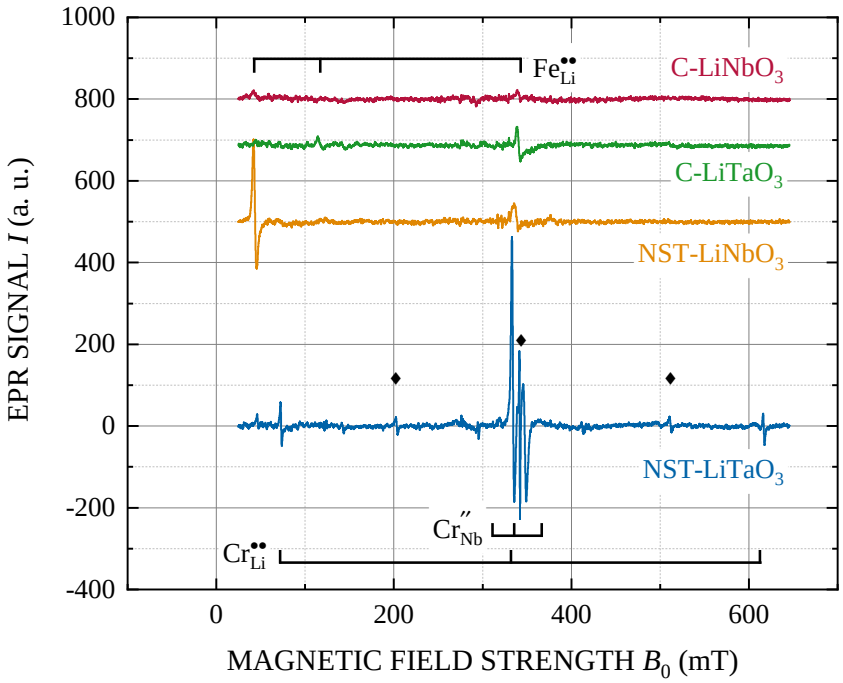


**Fig. S2** Recorded EPR spectra of $Cr^{3+}$ and $Fe^{3+}$ in as-grown NST- and C-Li$M$O$_3$ crystal plates with $\nu = 9.46$ GHz at room temperature. The crystallographic $c$ axis was parallel to the $B_0$ field. The black brackets indicate the dominant resonance lines of $Cr^{3+}$ and $Fe^{3+}$ on regular cation lattice sites; the symbol ♦ marks the corresponding satellite centres.

Fig. S2 shows the recorded EPR spectra for NST- and C-Li$M$O$_3$ crystal plates with $B_0$ parallel to the $c$ axis. It is obvious that the paramagnetic centres in the materials are different. As reported by GRACHEV et al.[19], the measured signals can be assigned to $Cr^{3+}$ and $Fe^{3+}$ impurities. $Cr^{3+}$ can be merely identified in NST-LiTaO$_3$ crystals, where the signals are intense and narrow. It is noticeable that due to the low intrinsic defect density in the NST-LiTaO$_3$ crystals, the resonance lines are particularly sharp and a much better resolution can be achieved[19,20]. Furthermore, it can be assumed that the concentration of paramagnetic impurities is higher than in the other crystalline samples. The resonance lines of $Cr^{3+}$ on Li sites are particularly dominant in the spectra. For charge neutrality, the trivalent ions can be compensated via $V'_{Li}$, $V''''''_{Nb}$, or by the formation of $Cr^{\bullet\bullet}_{Li}$–$Cr''_{Nb}$ pairs. For the NST crystals with a Li/Ta ratio of 0.998, a substitution of the Ta sites for charge compensation can be assumed and our measurements confirm this compensation model[19,21]. It should be noted that the $Cr^{\bullet\bullet}_{Li}$–$Cr''_{Nb}$ pairs, which occupy the nearest Li and Nb sites, are EPR silent, so there must be a compensation via the next order (long-range compensation), as shown by previous studies[22–24]. Furthermore, previous PIXE/channeling investigations[25] on low-doped C-LiNbO$_3$ show that the distribution of $Cr^{3+}$ on both cation sites is 60:40 for Li and Nb sites, respectively. It is therefore assumed that most of the chromium occurs as non-EPR active pair centres.

In contrast to the NST-LiTaO$_3$ crystals, we find predominantly $Fe^{3+}$ impurities for the other crystals in agreement with known literature[19]. It is assumed that $Fe^{3+}$ preferentially occupies the regular Li sites[26–30]. Within the investigated congruent crystal composition, a charge compensation can preferably occur with two $V'_{Li}$[19]. In the congruent crystals, the vacancy concentration is very high – 5.9 mol% and 2.2 mol% for C-LiNbO$_3$[12] and C-LiTaO$_3$[13], respectively – so that the paramagnetic impurities can be easily compensated. Only the transition to stoichiometric material allows self-compensation. In short: If the dopant concentration is lower than the intrinsic defect concentration, the latter can provide charge compensation and if the dopant concentration is dominant, self-compensation of the paramagnetic impurities is possible.

The occupation of paramagnetic impurities on Nb/Ta sites causes preferential decoration of hydrogen, which will be oriented in the O–O plane as a result[17,18]. As shown in Sec. 3.3.3, paramagnetic impurities cause some tilting of the O–H dipole moment out of the O–O plane. It can be concluded that the $Cr^{3+}$ and $Fe^{3+}$ impurities in the NST crystals cause the $OH^-$ defect to be located close to the O–O plane and not on the calculated *ab initio* positions, which are valid for impurity-free crystals.

## Notes and references


1 J. Herrington, B. Dischler, A. Räuber and J. Schneider, Solid State Communications, 1973, **12**, 351–354.
2 H. H. Nahm and C. Park, Applied Physics Letters, 2001, **78**, 3812–3814.
3 L. Kovács, V. Szalay and R. Capelletti, Solid state communications, 1984, **52**, 1029–1031.
4 K. Lengyel, L. Kovács, G. Mandula and R. Rupp, Ferroelectrics, 2001, **257**, 255–262.
5 Y. Kong, W. Zhang, X. Chen, J. Xu and G. Zhang, Journal of Physics: Condensed Matter, 1999, **11**, 2139.
6 A. Gröne and S. Kapphan, Journal of Physics and Chemistry of Solids, 1995, **56**, 687–701.
7 C. Bäumer, C. David, K. Betzler, H. Hesse, K. Lengyel, L. Kovács and M. Wöhlecke, physica status solidi (a), 2004, **201**, R13–R16.
8 T.-H. Kim, Y. M. Yu, O.-Y. Jeon, J. H. Ro, M. Cha and J.-H. Ro, Journal of the Korean Physical Society, 2002, **41**, 390–394.
9 A. Grone and S. Kapphan, Journal of Physics: Condensed Matter, 1995, **7**, 6393.
10 T. Köhler, E. Mehner, J. Hanzig, G. Gärtner, H. Stöcker, T. Leisegang and D. Meyer, Journal of Solid State Chemistry, 2016, **244**, 108 – 115.
11 L. Shi, W. Yan and Y. Kong, The European Physical Journal-Applied Physics, 2007, **40**, 77–81.
12 S. C. Abrahams and P. Marsh, Acta Crystallographica B, 1986, **42**, 61–68.
13 T. Köhler, M. Zschornak, M. Zbiri, J. Hanzig, C. Röder, C. Funke, H. Stöcker, E. Mehner and D. C. Meyer, Journal of Materials Chemistry C, 2021, **9**, 13484–13499.
14 A. Yatsenko, Physics of the Solid State, 1998, **40**, 109–111.
15 M. Paturzo, P. Ferraro, S. Grilli, D. Alfieri, P. De Natale, M. de Angelis, A. Finizio, S. De Nicola, G. Pierattini, F. Caccavale et al., Optics express, 2005, **13**, 5416–5423.
16 D. Orth, R. Mashl and J. Skinner, Journal of Physics: Condensed Matter, 1993, **5**, 2533.
17 L. Kovács, Z. Szaller, K. Lengyel and G. Corradi, Optical Materials, 2014, **37**, 55–58.
18 L. Kovács, L. Kocsor, É. Tichy-Rács, K. Lengyel, L. Bencs and G. Corradi, Optical Materials Express, 2019, **9**, 4506–4516.
19 V. G. Grachev and G. I. Malovichko, Crystals, 2021, **11**, year.
20 G. Malovichko, V. Grachev and O. Schirmer, Applied Physics B, 1999, **68**, 785–793.
21 V. Grachev, G. Malovichko and O. Schirmer, Ukrains'kyi Fizychnyi Zhurnal, 2004, **49**, 438–447.
22 G. Malovichko, V. Grachev, E. Kokanyan and O. Schirmer, Physical Review B, 1999, **59**, 9113.
23 V. Grachev, G. Malovichko and O. Schirmer, Ferroelectrics, 1996, **185**, 5–8.
24 G. Siu and Z. Min-Guang, Physical Review B, 1991, **43**, 13575.
25 A. Kling, J. Soares, M. Da Silva, J. Sanz-García, E. Dieguez and F. Agullo-Lopez, Nuclear Instruments and Methods in Physics Research Section B: Beam Interactions with Materials and Atoms, 1998, **136**, 426–430.
26 H. Sothe, L. Rowan and J.-M. Spaeth, Journal of Physics: Condensed Matter, 1989, **1**, 3591.
27 H. Sothe and J.-M. Spaeth, Journal of Physics: Condensed Matter, 1992, **4**, 9901.
28 T. Gog, P. Schotters, J. Falta, G. Materlik and M. Grodzicki, Journal of Physics: Condensed Matter, 1995, **7**, 6971.
29 G. Corradi, A. Chadwick, A. West, K. Cruickshankand and M. Paul, Radiation effects and defects in solids, 1995, **134**, 219–222.
30 L. Rebouta, M. Da Silva, J. Soares, M. Hage-Ali, J. Stoquert, P. Siffert, J. Sanz-García, E. Dieguez and F. Agulló-López, EPL (Europhysics Letters), 1991, **14**, 557.